Models of non-Boussinesq lock-exchange flow

By R. ROTUNNO [1] **, J. B. KLEMP** [1] **, G. H. BRYAN** [1]
AND D. J. MURAKI [2]

[1]National Center for Atmospheric Research*, Boulder, CO 80307

[2]Department of Mathematics, Simon Fraser University, Burnaby, BC V5A 1S6, Canada

Nearly all analytical models of lock-exchange flow are based on the shallow-water approximation. Since the latter approximation fails at the leading edges of the mutually intruding fluids of lock-exchange flow, solutions to the shallow-water equations can be obtained only through the specification of front conditions. In the present paper analytic solutions to the shallow-water equations for non-Boussinesq lock-exchange flow are given for front conditions deriving from free-boundary arguments. Analytic solutions are also derived for other proposed front conditions—conditions which appear to the shallow-water system as forced boundary conditions. Both sets of solutions to the shallow-water equations are compared with their counterparts from the Navier-Stokes equations and a mixture of successes and failures is recorded. The apparent success of some aspects of the forced solutions of the shallow-water equations, together with the fact that in a real fluid the density interface is a free boundary, shows the need for an improved theory of lock-exchange flow taking into account nonhydrostatic effects for density interfaces intersecting rigid boundaries.

1. Introduction

Lock-exchange flow results from the adjustment under gravity of two fluids of different densities initially separated by a vertical partition in a horizontal channel (Fig. 1a). In addition to gravity and pressure-gradient forces, a model of lock-exchange flow must reckon with stress at the channel walls, stress and diffusion between the two fluids and, in cases involving a liquid-gas interface, surface-tension effects. Given the mathematical complexity attaching to these processes, the more tractable two-layer shallow-water equations, in which the aforementioned processes are either neglected or simply represented, have been applied to lock-exhange flow by Rottman and Simpson (1983; RS), Keller and Chyou (1991; KC), Klemp, Rotunno and Skamarock (1994; KRS), Shin, Dalziel and Linden (2004) and Lowe, Rottman and Linden (2005; LRL) among others. Judging the relative merits of these differing applications of the shallow-water equations against laboratory data is difficult owing to the influence of the aforementioned neglected effects. However the gap between shallow-water theory and laboratory experiments can be bridged in certain cases by using numerical integrations of less approximate fluid-flow equations as surrogates for laboratory data (KRS; Birman, Martin and Meiburg 2005). In this article we extend the Boussinesq (density ratio of lighter to heavier fluid $r \approx 1$) two-layer shallow-water theory put forward by KRS to the non-Boussinesq case and then evaluate it and another shallow-water theory against compatible (i.e. free-slip, no surface-tension, etc.) numerical integrations of the Navier-Stokes equations for lock-exchange flow.

As the shallow-water equations (SWE) are based on the hydrostatic approximation, they are incapable of describing flow with strong horizontal variation, such as at the leading edges of the mutually intruding interfaces shown in Fig. 1a. In order to use the SWE in such cases, one admits solution discontinuities and appeals to a more complete physical theory for conditions that apply across them. RS proposed using a formula developed by Benjamin [1968, his Eq. (2.22)] to relate the right-going front speed $\tilde{u}_f$ to its depth $\tilde{h}_f$ in a Boussinesq 'dam-break' calculation using the two-layer SWE. Benjamin's formula, based on mass and momentum balance across a control volume moving with a steadily propagating gravity current (e.g. Simpson and Britter 1979), gives $\tilde{u}_f$ in terms of the height $\tilde{h}_f$ of the lower fluid well behind the complex flow of the gravity-current head; in solutions of the SWE, Benjamin's control volume containing the gravity-current head is represented by a simple discontinuity as shown in Fig. 1b. In their application of the two-layer SWE to the Boussinesq lock-exchange problem, RS found that the left-going interface (Fig. 1a), which was left to evolve freely, immediately became multi-valued (RS's Fig. 7c). KRS resolved the latter problem by recognizing that the left-going interface must also be represented by a discontinuity that satisfies Benjamin's (1968) front condition (Fig. 1b); Fig. 7d of KRS gives the solution of the SWE for the lock-exchange problem in the Boussinesq limit.

A continuing source of discussion in the literature is that the Benjamin front condition admits a special dissipation-free solution along with a continuum of solutions having dissipation. KRS pointed out that the dissipation-free front condition in the SWE would imply a front speed that is greater than the speed at which information can travel to it from
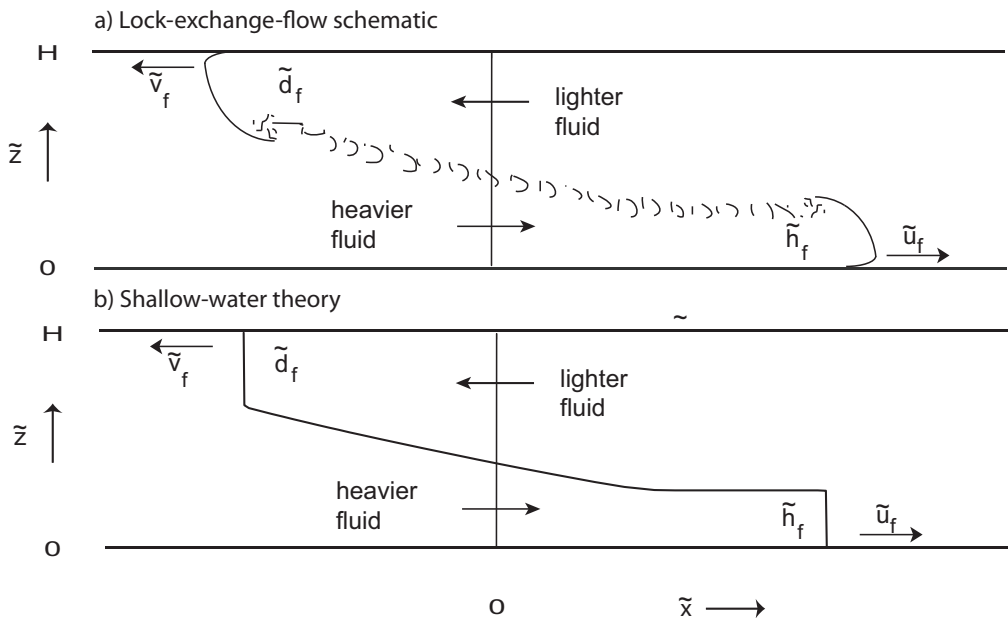

FIGURE 1. Schematic of lock-exchange flow based on a) laboratory data and b) typical solutions to the shallow-water equations. The vertical line at $\tilde{x} = 0$ indicates the lock center where the heavier and lighter fluids are initially separated; the horizontal channel walls are separated in the vertical by a distance H. After the release of the lock the heavier (lighter) fluid flows to the right (left) at speed $\tilde{u}_f$ ($\tilde{v}_f$) with thickness $\tilde{h}_f$ ($\tilde{d}_f$) measured some distance behind the complicated flow at the leading edge.

the lock center (violating 'causality') in both the Boussinesq ($r \approx 1$) and cavity ($r \to 0$) limits (see KRS's Fig. 3). On the other hand some laboratory investigators promote the relevance of the dissipation-free front condition to experimental flows (e.g. Shin et al. 2004), while other laboratory experiments (Simpson and Britter 1979) and numerical experiments (see Fig. 14 of Hartel, Meiburg and Necker 2000 or Fig. 16d of Bryan and Rotunno 2008) find flows consistent with a dissipative front condition for Boussinesq lock-exchange flow. For non-Boussinesq conditions ($r < 1$), laboratory experiments (KC; Gröbelbauer, Fanneløp and Britter 1993; LRL) and numerical simulations (Birman *et al.* 2005; Étienne *et al.* 2005; Bonametti *et al.* 2008) show that as r decreases from unity, the right-going front of relatively heavy fluid increases in speed and becomes more turbulent, while the speed of the left-going front of relatively light fluid remains unchanged and becomes less turbulent.

This latter feature led KC to consider the left-going front as the realization of the dissipation-free Benjamin front condition. Following KC, LRL used two-layer shallow-water theory to construct the solution between the dissipation-free left-going upper front and a right-going front obeying the (generally dissipative) Benjamin front condition across the range of r (Fig. 4b of LRL). The 'causality' problem raised by KRS of the impossibility of information flow in the SWE from lock center to the dissipation-free front was not addressed.

In the present paper we extend the KRS Boussinesq two-layer shallow-water theory to apply across the range of r. As in KRS, the present theory is based on the two-layer SWE and the application of the Benjamin front condition to the left- and right-going fronts, respectively. As with the KRS numerical integrations of the SWE in the Boussinesq limit, the present non-Boussinesq solutions require the dissipative Benjamin front condition across the range $0 \leq r \leq 1$ for solutions that obey causality. We then verify that these numerical solutions are unique through an independent, exact analysis using the method of characteristics. For comparison with the present solutions, we have also constructed analytical solutions following the LRL approach described above. These exact solutions offer a mathematically firm explanation for the numerical-solution features such as the apparent 'expansion fans' and 'zones of constant state' that appear. Perhaps more important is that the exact analysis gives a clear picture of information flow through the system as seen by the shallow-water theory.

To evaluate the present and the LRL SWE solutions, we have carried out two- and three-dimensional numerical simulations using the Navier-Stokes (NS) equations. The simulations are carried out under free-slip conditions at the channel walls and without surface-tension effects. One effect contained in the NS equations but not in the SWE is interfacial instability; hence viscous effects are unavoidable as they effect the growth and ultimate disposition of unstable waves growing on the interface. As pointed out by Benjamin (1968, p. 224-225) the upper gravity current is completely stable as $r \to 0$ while it is unstable to disturbances of all wavelengths as $r \to 1$; on the other hand the lower gravity current is unstable at any r. Consistent with the foregoing arguments, the present numerical solutions indicate that the character (laminar or turbulent) of the upper front is a function of both r and the relative strength of viscous effects through the Reynolds number Re. For $Re > Re_{cr}(r)$, where $Re_{cr}(r)$ is the critical value for transition to turbulence, we find better agreement between the NS solutions with the present extension of the KRS theory than with the LRL theory; however for $Re < Re_{cr}$, the numerical solutions indicate better agreement with the LRL theory than with the present one.

Hence we are led to the conclusion that for $Re < Re_{cr}(r)$, the solution to the Navier-Stokes equations for the lock-exchange problem is outside the SWE solution space for solutions respecting the causality condition. Our exact analysis of the LRL SWE solutions indicates that all information flows from left-going dissipation-free front inward towards the lock center. From the point of view of the SWE, the left-going front must thus be viewed as an external agent; that is, the mathematical problem becomes a forced- (rather than a free-) boundary problem.

Numerical solutions of two-layer SWE for non-Boussinesq lock-exchange flow are described next in Section 2. Motivated by these numerical solutions, which are consistent with information flow from the lock center outward, Section 3a describes an exact 'causal' analytical solution to SWE using the method of characteristics. For reasons listed above, we give in Section 3b, analytical solutions of the SWE for prescribed frontal parameters at the left-going front of lighter fluid; these solutions do not respect 'causality' but may nonetheless be useful descriptions of fluid flow features that are beyond shallow-water theory. Section 4 compares the SWE solutions to those of the less-approximate NS equations and, in particular, examines the variation of the solutions with both density ratio r and Re. A summary and concluding remarks are given in Section 5.

2. Numerical Solution of the Two-Layer Shallow Water Equations

Following RS, KC and LRL, the two-layer SWE equations for flow in a horizontal channel neglecting stress, diffusion and surface tension, can be written in terms of the lower-layer height and velocity; in nondimensional form these are

$$\frac{\partial h}{\partial t} + u\frac{\partial h}{\partial x} + h\frac{\partial u}{\partial x} = 0 \tag{2.1}$$

and

$$\frac{\partial u}{\partial t} + a\frac{\partial u}{\partial x} + b\frac{\partial h}{\partial x} = 0, \tag{2.2}$$

where

$$a = u\frac{(1-h)^2 - rh(1+h)}{(1-h)^2 + rh(1-h)} \quad \text{and} \quad b = \frac{(1-h)^3 - ru^2}{(1-h)^3 + rh(1-h)^2} \quad . \tag{2.3a,b}$$

In (2.1)-(2.3), $h = \tilde{h}/H$ and $u = \tilde{u}/\sqrt{g'H}$, where $\tilde{h}$ is the depth, and $\tilde{u}$ the velocity, of the lower layer; the independent variables are $x = \tilde{x}/H$ and $t = \tilde{t}\sqrt{g'/H}$; the reduced acceleration due to gravity is defined by $g' = (1-r)g$. For future reference, note that $d = \tilde{d}/H = 1 - h$ and, by continuity, $v = \tilde{v}/\sqrt{g'H} = -uh/d$. The initial condition is $u(x,0) = 0$, and $h(x,0) = 1$ for $x \leq 0$ and $h(x,0) = 0$ for $x > 0$.

As mentioned in the Introduction, RS used a front condition to represent the gravity current at the leading edge of the right-going fluid in a Boussinesq shallow-water calculation, while the left-going intrusion was left to evolve freely. As evidenced by the result of that calculation (RS's Fig. 7c), $h(x,t)$ for the left-going interface immediately became multi-valued for $t > 0$. KRS demonstrated, through an evaluation of the wave-propagation characteristics at the leading edge of the disturbance propagating to the left, that deeper heights travel slower than shallower heights; hence multi-valued solutions are to be expected, and the application of a front condition is required. For the present non-Boussinesq case, the wave propagation in system (2.1)-(2.2) is given by

$$c^{\pm} = \frac{1}{2}(u + a) \pm \frac{1}{2}\sqrt{(u+a)^2 - 4(au - bh)} \tag{2.4}$$

[LRL's Eq. (3.13)]; setting $u = 0$ in (2.4) gives

$$c^- \approx -\sqrt{\frac{h(1-h)}{1-(1-r)h}} \qquad (2.5)$$

for a disturbance propagating toward the quiescent fluid to the left of the partition. In the Boussinesq limit, $r = 1$ and KRS's (23) is recovered showing that lower heights travel to the left faster than higher ones for $h > h_{cr} = 0.5$. Equation (2.5) shows that lower heights travel faster than higher heights for $h > h_{cr}(r)$ (where $h_{cr}(r)$ increases from a value of 0.5 with decreasing r) for any finite $r \neq 0$ and hence there is the necessity for a front condition. We note in passing that (2.5) illustrates just one of the many intricacies associated with a *moving contact line* (Shikhmurzaev, 2008, Chapter 5). In the foregoing argument we are implicitly considering the limits $h \to 1$ (lock exchange) and $r \to 0$ (cavity) in that order. Taking the limits in the reverse order gives the classical one-layer result $c^- = -\sqrt{h}$ implying that that the lower fluid takes no notice of the upper fluid, and therefore, of the upper bounding surface.

Following Benjamin (1968), application of mass and momentum conservation across the front of each gravity current gives

$$v_f = -\sqrt{\frac{d_f(2-d_f)(1-d_f)}{1+d_f}} \quad , \qquad (2.6)$$

for the left-going front, and

$$u_f = \sqrt{\frac{1}{r}\frac{h_f(2-h_f)(1-h_f)}{1+h_f}} \quad . \qquad (2.7)$$

for the right-going front.

With the front conditions (2.6)-(2.7), numerical solutions of (2.1)-(2.2) are computed across the range of r and shown in Fig. 2. Figures 2a, c and e show snapshots at $t = 10$ of the interface height $h(x)$ for $r = 1.0, 0.7$ and 0.4, respectively, while Figs. 2b, d and f show the corresponding velocities $u(x)$ and $v(x)$ in the lower and upper layers, respectively. For the Boussinesq case (Figs. 2a, b), the solution has the required reflective symmetry [$h(x) = d(-x)$, $u(x) = -v(-x)$]; the frontal parameters, $h_f = d_f = 0.3473$ and $u_f = -v_f = 0.527$ (cf. KRS's Fig. 7d). For the density ratio $r = 0.7$, Fig. 2c indicates that $h(x)$ is no longer symmetric, although the front heights are still equal to their values in the $r = 1$ case (Fig. 2a). Moreover the velocity distributions (Fig. 2d), indicate that the lower-fluid front speed has increased, while that of the upper fluid has remained as it was in the $r = 1$ case (Fig. 2b). With the density ratio reduced to $r = 0.4$, Fig. 2e indicates no change in the thickness d_f of the left-going front, while that of the right-going front h_f is reduced, with respect to the $r = 1.0$ and 0.7 cases; the velocity distributions in Fig. 2f indicate a further speed increase of the right-going front, but no change in that of the left-going front. In contrast with the $r = 1.0$ and 0.7 cases, the case with $r = 0.4$ has both h and u independent of x for some distance behind the right-going front.

To aid in the interpretation of the numerical solutions shown in Fig. 2, we examine the corresponding characteristic velocities $c^\pm(u, h)$ given by (2.4). Figure 2b shows for the $r = 1.0$ case that $0 < c^+ \leq u$ and, by symmetry, $v \leq c^- < 0$. With the density ratio
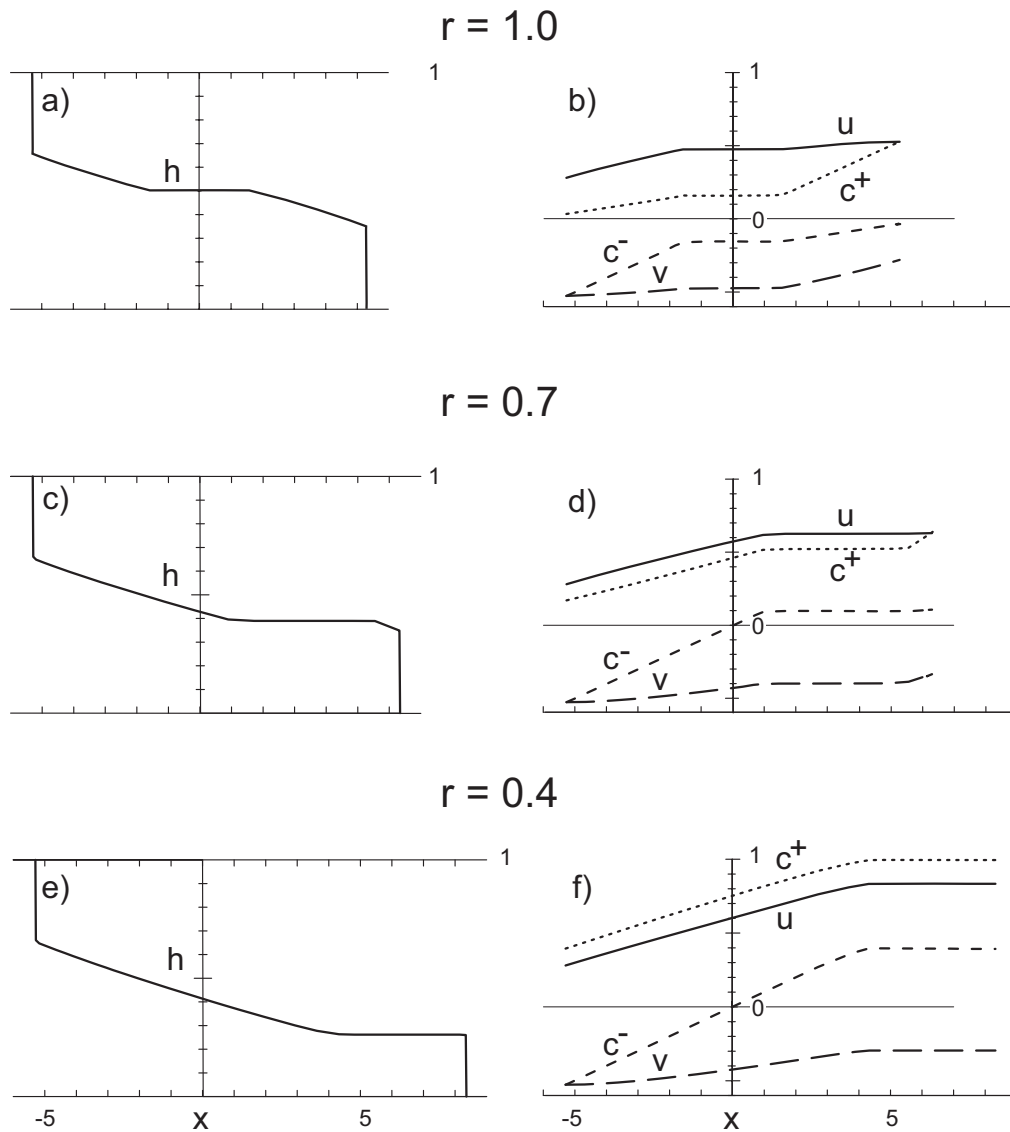
FIGURE 2. Numerical solutions of the two-layer shallow water equations with the front conditions (2.6)-(2.7) for $r = 1.0, 0.7$ and 0.4. For each r, the height of the interface is displayed in a), c) and e), and the layer and characteristic velocities (2.4) are displayed in b), d) and f).

$r = 0.7$, Fig. 2d shows that, as in the case with $r = 1.0$, $0 < c^+ \leq u$, but that c^+ is closer in magnitude to u throughout the interval between the fronts. On the other hand for c^-, Fig. 2d for $r = 0.7$ shows that $v \leq c^- \leq 0$ for $x \leq 0$ and that $c^- \geq 0$ for $x \geq 0$, indicating that no information can travel from the right to the left of $x = 0$. At a density ratio of $r = 0.4$, Fig. 2f shows that $c^+ > u$, while the distribution of c^- is qualitatively the same as for the $r = 0.7$ case.

3. Solutions of the SWE by the Method of Characteristics

The solution to the lock-exchange problem shares with the classical piston and dam-break problems the property that the governing equations, front conditions, and the initial conditions are without any implied space or timescales. As a result, for $t > 0$, solutions must only depend on the similarity variable x/t, and the time evolution is simply a linear-in-time dilatation of the spatial structure. In this section, the spatial structure, as a function of x/t, is determined by the method of characteristics.

The hyperbolic equations (2.1)-(2.2) can be written as

$$\begin{pmatrix} h \\ u \end{pmatrix}_t + \begin{bmatrix} u & h \\ b & a \end{bmatrix} \begin{pmatrix} h \\ u \end{pmatrix}_x = \vec{0} \tag{3.1}$$

where the characteristic velocities $c^\pm$ (2.4) are obtained as the eigenvalues of the matrix. Multiplication by the left-eigenvector $(a - c^\pm, -h)$ gives the Riemann invariant relation

$$(a - c^\pm)\frac{dh}{dt} - h\frac{du}{dt} = 0 \tag{3.2}$$

where the derivatives are along characteristic trajectories (or 'rays') defined by $dx^\pm/dt = c^\pm$. As the Riemann invariant relation has no explicit dependence on x or t, it can be integrated as the ordinary differential

$$\frac{du^\pm}{dh} = \frac{a - c^\pm}{h}, \tag{3.3}$$

giving the dependence of $u^\pm(h)$ along the ray $x^\pm(t)$. In the present application we will be concerned with solutions of (3.3) with starting values for (u^+, h) given by the left-going frontal parameters (u_L, h_L) and for (u^-, h) given by the right-going frontal parameters (u_R, h_R).

a. Free-boundary solutions

The locations of the left- and right-going fronts that delimit the propagation of the lock-exchange flow into regions of the quiescent fluid are determined here by free-boundary arguments. First, conservation of mass dictates that the fronts move with the fluid speed; hence, on a ray diagram, the right-going front is the event line $x/t = u_R$, and the left-going front is the event line $x/t = v_L$. Second, the assumption that the Benjamin relation applies provides another condition: $\sqrt{r}u_R = \mathcal{B}(h_R)$ (2.7) for the right-going and $v_L = -\mathcal{B}(d_L)$ (2.6) for the left-going front. Determination of both frontal variables, (u_R, h_R) or (v_L, d_L), requires a third condition. There are two possible scenarios for completing the front specification, and we refer to these as the *characteristic Benjamin front* and the *time-like Benjamin front*. These are defined below, where the right-going front is considered first.

The right-going front speed must satisfy the inequality

$$c_R^- < u_R \le c_R^+ \tag{3.4}$$

to satisfy 'causality', that is, forbidding the front to propagate faster than the right-going characteristic speed, and requiring that the front have influence on the trailing region of disturbed fluid. The case of equality in (3.4) defines the characteristic Benjamin front,

where the event line coincides with the right-going characteristic line. In this case, the third front condition is

$$u_R = c_R^+ = c^+(u_R, h_R; r) \, . \tag{3.5}$$

It follows from the characteristic equation (2.4) that (3.5) is satisfied only when the coefficient $b(u_R, h_R; r) = 0$, so that from (2.3b),

$$r \, u_R^2 = (1 - h_R)^3 \, . \tag{3.6}$$

Simultaneous solution of (3.6) with the Benjamin front condition (2.7) gives the unique solution

$$\sqrt{r} \, u_R \approx 0.5273 \quad ; \quad h_R \approx 0.3473 \tag{3.7}$$

for the frontal parameters. It may be verified from (2.4) that for frontal parameters (3.7), $c_R^- < c_R^+$, as required by (3.4).

For the time-like Benjamin front, the frontal parameters are determined by a third condition that is dictated by an inbound (from the left) characteristic. In this case the front speed u_R satisfies the strict inequality

$$c_R^- < u_R < c_R^+ \tag{3.8}$$

implying that the c^+-rays from the left-going front now propagate through the disturbed fluid and intersect the right-going front. Therefore in this case the right-going front parameters (u_R, h_R) derive from the solution of (3.3) for $u^+(h)$ for rays emanating from the left-going front together with the condition (2.7).

Turning now to the left-going front, the inequality analogous to (3.4) is

$$c_L^- \leq v_L < c_L^+ \, . \tag{3.9}$$

A left-going characteristic Benjamin front is thus defined by

$$v_L = c_L^- = c^-(u_L, h_L; r) \tag{3.10}$$

and gives the third determining condition. Following the same logic as for the right-going front, the condition (3.10) leads to the relation

$$v_L^2 = (1 - d_L)^3 \tag{3.11}$$

in analogy with (3.6). For the left-going characteristic front then, combining (3.11) with the Benjamin front condition (2.6) gives the numerical solution for the frontal parameters

$$v_L \approx -0.5273 \quad ; \quad d_L \approx 0.3473 \tag{3.12}$$

in analogue with (3.7) except in this case the result is independent of r. The upper-fluid values (3.12) correspond to the lower-fluid values

$$u_L \approx 0.2806 \quad ; \quad h_L \approx 0.6527 \, . \tag{3.13}$$

There is also the possibility for a left-going time-like Benjamin front. In this case, the third condition would be obtained by an inbound characteristic (from the right). Our calculations of c_L^- using $u_L = u^-(h_L)$ from the solution of (3.3) show, however, that there are no solutions for which the case of $c_L^- < v_L$ is physically realized. The analysis

of c^- from the numerical SWE solutions shown in Figs. 2d and f is consistent with this result.

We are now ready to construct solutions to the SWE by the method of characteristics and begin with the Boussinesq case ($r = 1.0$). As a starting point we assume that both left- and right-moving fronts are of the characteristic Benjamin type and that therefore on a ray diagram the region of disturbed flow lies inside the cone $c_L^- \leq x/t \leq c_R^+$. Figure 3a shows the Riemann invariant $u^-(h)$ that emanates from the right-moving front [where $(u^-, h) = (u_R, h_R)$ given by (3.7)] together with the Riemann invariant $u^+(h)$ that emanates from the left-going front [where $(u^+, h) = (u_L, h_L)$ given by (3.13)]. There is a unique crossing point where $u^+(h_c) = u^-(h_c) = u_c$, where $u_c \approx 0.44$ and $h_c = 0.5$. This crossing point thus defines two cones of influence on a ray diagram: the right-moving front influences the region $c_c^- \leq x/t \leq c_R^+$ while the left-moving front influences the region $c_L^- \leq x/t \leq c_c^+$, where $c_c^- = c^-(u_c, h_c)$ and $c_c^+ = c^+(u_c, h_c)$. The overlapping zones of influence thus define a cone $c_c^- \leq x/t \leq c_c^+$ where $h = h_c$ and $u = u_c$, i.e, a "zone of constant state". Referring to Fig. 4a, the upper panel shows this "zone of constant state" (thin line segment) in terms of $h(x/t)$ and corresponds to the cone $c_c^- \leq x/t \leq c_c^+$ in the ray diagram directly below. The other curves in Fig. 3a are the characteristic velocities and the upper-layer velocities corresponding to their respective Riemann invariant velocities $u^\pm$ between their respective launch points and the crossing point. Figure 3a indicates that the region $v_L \leq x/t \leq c_c^-$ is uninfluenced by the $u^-(h)$ Riemann invariant and hence that region must be an expansion fan. The solution $h(x/t)$ can be deduced parametrically from

$$x/t = c^-[u^+(h)] . \tag{3.14}$$

Likewise the region $c_c^+ \leq x/t \leq u_R$ is also an expansion fan with the solution given parametrically by

$$x/t = c^+[u^-(h)] . \tag{3.15}$$

The solution $h(x/t)$ for these two expansion fans is shown by the thick line segments in the upper panel of Fig. 4a. Finally, the rays are computed and shown as thin lines in the lower panel of Fig. 4a. It may be verified that the analytical solution for $h(x/t)$ shown in Fig. 4a is essentially identical to the numerical solution shown in Fig. 2a.

Following the same procedure as for the Boussinesq case, we next construct the solution for the non-Boussinesq case $r = 0.7$. Figure 3b shows that the r-dependence in the right-going front speed (2.7) produces an upward shift in $u^-(h)$ so that the intersection with the (unchanged) $u^+(h)$ shifts to $h_c \approx 0.3907$. Otherwise the logic of the solution construction is identical to the Boussinesq case, and is illustrated in Fig. 4b. In this case with $r = 0.7$, the zone of constant state shifts towards the right-going front and there is a narrowing of the right-going expansion fan. Again the analytical solution for $h(x/t)$ shown in the upper panel of Fig. 4b is essentially identical in every detail to the numerical solution shown in Fig. 2b,

With further decreases in r, the right-going expansion fan is eventually eliminated at a critical value of r where $c_c^+ = u_R$. At this critical value of r_{cr} (≈ 0.5821) however, the solution must undergo a change of spatial character. For $r < r_{cr}$, the intersection of the two Riemann invariant curves $u^+(h)$ and $u^-(h)$ occurs at $h < 0.3473$ which is less than the value for the right-going characteristic Benjamin front. In addition, it is also found that c_c^+ would exceed the propagation speed u_R of the assumed characteristic Benjamin front. The resolution of these conflicts is that the right-going front parameters now satisfy the time-like condition (3.8). Figure 3c shows the $u^+(h)$ Riemann invariant curve extended
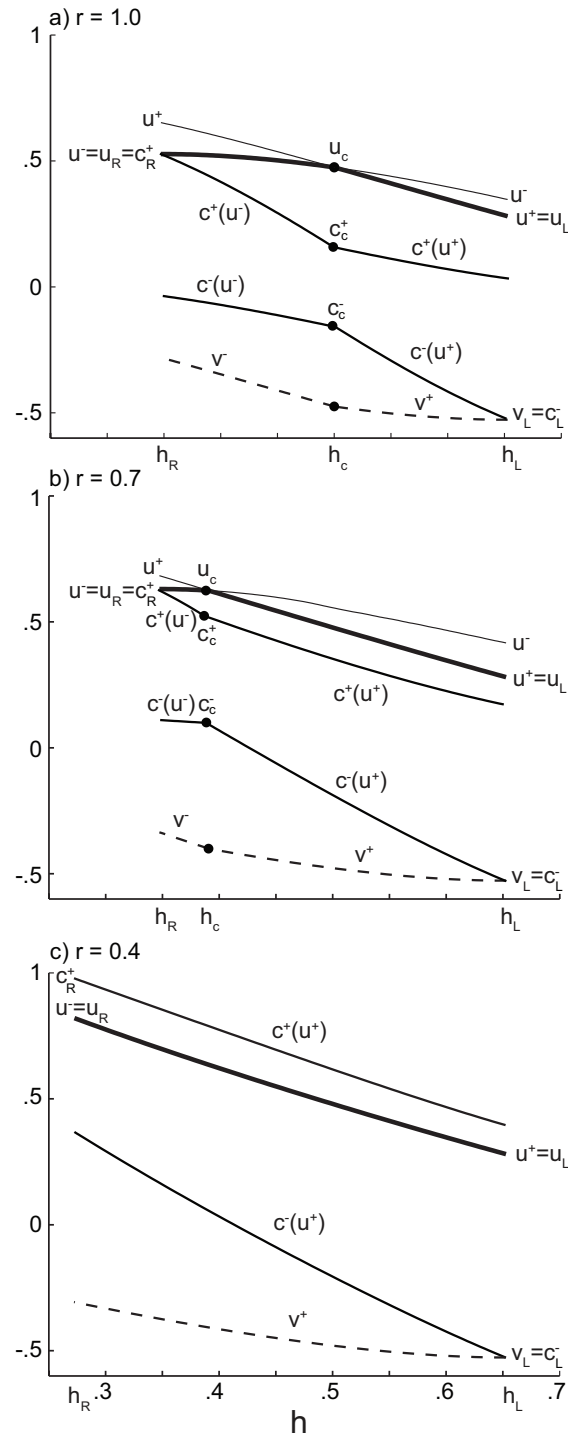
FIGURE 3. Solution to the Riemann invariant equation (3.3) for $u^{\pm}(h)$ for density ratio $r = $ a) 1.0. b) 0.7 and c) 0.4. Starting values for the integrations of (3.3) are indicated by the points $u^{-} = u_R, h = h_R$ and $u^{+} = u_L, h = h_L$. In a) and b), (u_C, h_C) denotes the crossing point where $u^{+}(h) = u^{-}(h)$ and the thick solid lines indicates the parts of the $u^{\pm}(h)$ solution curves relevant for calculating the corresponding characteristic velocities $c^{\pm}(u^{+})$, $c^{\pm}(u^{-})$ and upper-layer velocities $v^{\pm}$ (long-dashed curves). In c) there is no crossing point which indicates a change in character of the solution.
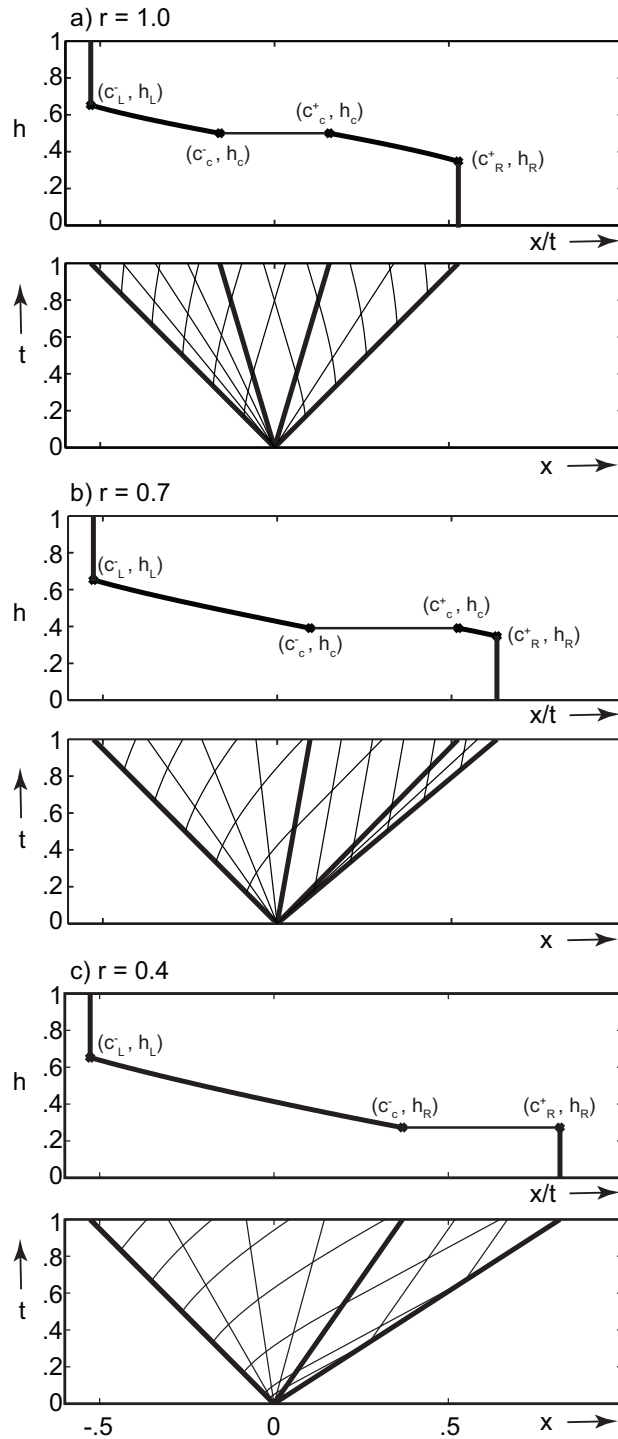
FIGURE 4. Analytical construction of the solution to the shallow water equations for density ratio $r =$ a) 1.0, b) 0.7 and c) 0.4. For each case the height of the interface h (upper panel) is plotted versus the combined coordinate x/t with the corresponding ray diagram given directly below. In a) and b) the zone of constant state where $h(x/t) = h_C$ (thin line segment) is located within the cone $c_C^- < x/t < c_C^+$ indicated in the ray diagram, and the left and right-side expansion fans (thick line segments) are defined by the ray-diagram cones $c_L^- < x/t < c_C^-$ and $c_C^+ < x/t < c_R^+$, respectively. In c) the right-side expansion fan disappears.

to the value $h_R \approx 0.2725$ which, with $u_R \approx 0.8203$, also satisfies the Benjamin front condition (3.7). The right-going front conditions are now also constant-state conditions. Figure 4c (lower panel) illustrates how the disappearance of the right-moving expansion fan also requires that rays launched from the left-going front to catch up to the right-going front as inbound rays. All rays of the c^- type carry constant values of h and u. We note that for $r < r_{cr}$ the ray diagram is analogous to that of the classic "dam-break" problem (Whitham 1974). As with the previous two cases the analytical solution for the height $h(x/t)$ in the upper panel of Fig. 4c matches the numerical solution shown in Fig. 2c.

A summary of the right-going frontal values of h_R and u_R are shown in Fig. 5. Solutions for $r > r_{cr} \approx 0.5821$ have a characteristic Benjamin front, while for $r < r_{cr}$ have a time-like Benjamin front. As can be inferred from Fig. 4, there are two critical features that coincide at the value r_{cr}: (a) as $r \to r_{cr}$ from above, $c_c^+ \to u_R$ (right-going expansion fan disappears); and (b) as $r \to r_{cr}$ from below, $c_R^+ \to u_R$ (rays emanating from left-going front become parallel to right-going-front event line). These conditions imply that the solutions represented in Fig. 5 are the unique solutions assuming a left-going characteristic Benjamin front and continuous solutions on $v_L \leq x/t \leq u_R$. Solutions for all r have a left-going characteristic Benjamin front with frontal parameters given by (3.12)-(3.13).

Solutions assuming a left-going time-like Benjamin front do not lead to a consistent construction of a spatial structure. Consider first the hypothetical case of a right-going time-like Benjamin front together with a left-going time-like Benjamin front: this case would give rise to a contradiction because both Riemann invariants $u^\pm(h)$ cannot satisfy the same end conditions $u^\pm(h_R) = u_R$ and $u^\pm(h_L) = u_L$ [since $c^-[u^-] \neq c^+[u^+]$, the '+' and '-' members of (3.30) are different]. In the hypothetical case of a right-going characteristic Benjamin front together with a left-going time-like Benjamin front, the latter would require $c_L^- < v_L$ (rays emanating from right-going front intersect the left-going front) which occurs only for the unphysical parameter regime $r > (r_{cr})^{-1} > 1$. Thus, the characteristic solutions as described here are the unique nonlinear solutions that are continuous on $v_L \leq x/t \leq u_R$.

b. Forced-Boundary Solutions

In this subsection we analyze the case considered by LRL of a dissipation-free, left-going front characterized by the front conditions

$$v_L = -u_L = -1/2 \quad ; \quad d_L = h_L = 1/2 \tag{3.16}$$

satisfying the Benjamin relation (2.6). The characteristic speeds (2.4) associated with these conditions satisfy the inequality $v_L < c_L^- < c_L^+$, and hence the rays from the left-going front are both directed into the lock exchange region implying that the frontal motion is not influenced by the flow within the lock region. Therefore, from the point of view of the SWE, (3.16) violates 'causality' as defined above (for further discussion, see §4*b*) and (3.16) must be considered a forced-boundary condition. The latter acts mathematically similarly to an initial condition and is commonly referred to as a *space-like* curve (ref Whitham) on a ray diagram.

The construction of solutions to the SWE by the method of characteristics presented above is changed only in that conditions (3.12)-(3.13) are replaced by (3.16). For the range of values $0 \leq r < r_{cr1} \approx 0.5532$, the Riemann invariant analysis leads to the right-going front being of the time-like Benjamin type. As seen in the example shown for $r = 0.4$ in Fig. 6a, the spatial profile has a constant-state generated by the propagation
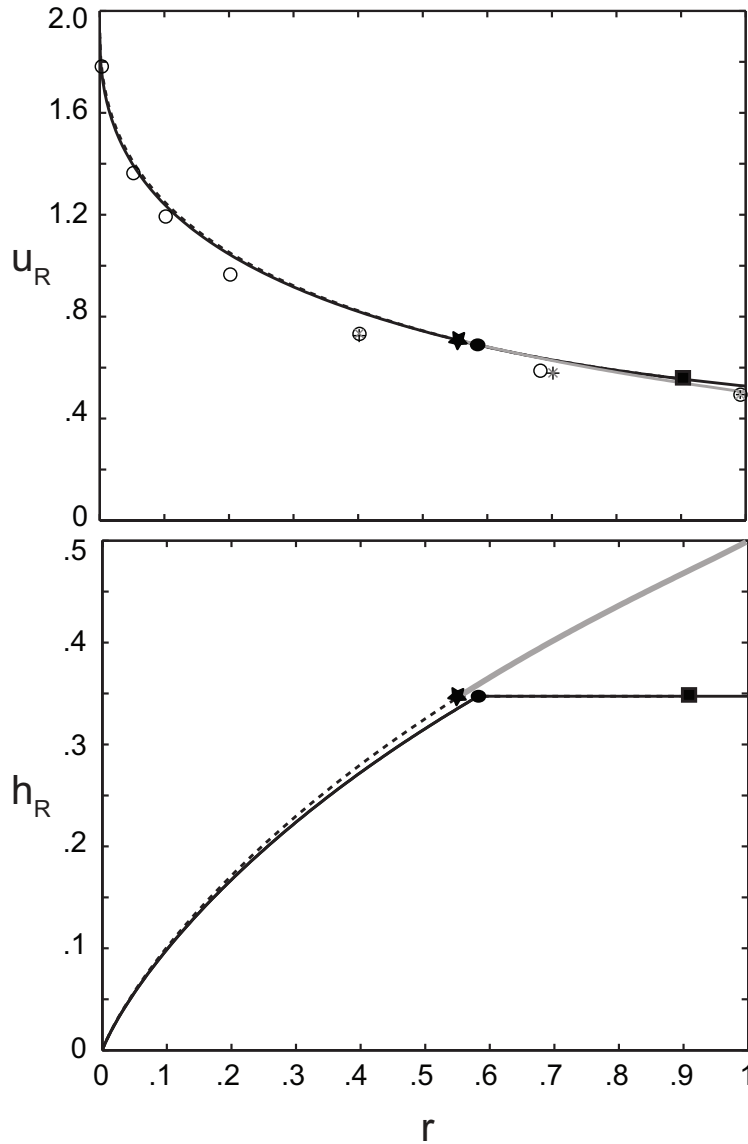
FIGURE 5. Right-side-front a) speed u_R, and b) height h_R, as a function of r. The present free-boundary solution (solid line) has two seqments separated by the dot at $r = r_{cr} = 0.5821$ indicating the density ratio dividing characteristic ($r > r_{cr}$) from time-like ($r < r_{cr}$) Benjamin fronts. Solutions with the forced-boundary condition $u_L = h_L = 1/2$ and free-boundary conditions for the right-side front (dashed line) have $r = r_{cr1} = 0.5532$ indicated by the star; the square at $r = r_{cr2} = 0.8953$ is the limiting density ratio beyond which continuous solutions do not exist for these assumed frontal conditions. The LRL solutions are same as the foregoing for $r < 0.5532$ but differ for $r > 0.5532$ (indicated by the solid gray line). The front-speed data from the present simulations are indicated by the '+' (2D) and the gray '×' (3D); data from the 2D simulations of Bonometti et al. (2008) are indicated by the circles.

a) r = 0.4 , (v_L , h_L)=(-0.5,0.5)

b) r = 0.7 , (v_L , h_L)=(-0.5,0.5)

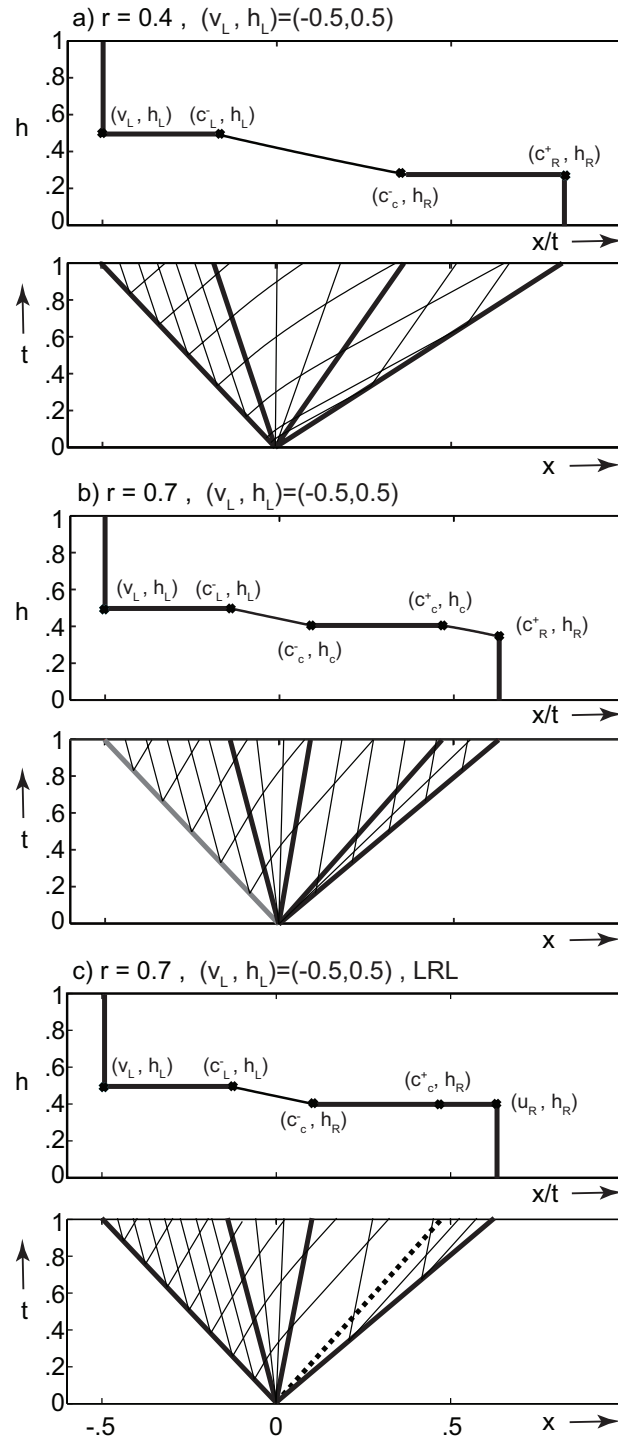c) r = 0.7 , (v_L , h_L)=(-0.5,0.5) , LRL

FIGURE 6. Analytical construction of the solution to the shallow water equations for the forced boundary condition $u_L = h_L = 1/2$ and free-boundary conditions on the right-side front for a) $r = 0.4$ and b) $r = 0.7$; c) LRL solution for $r = 0.7$ with forced-boundary conditions at both left and right fronts.

of the left-going dissipation-free front for $-1/2 < x/t < c_L^-$ (note that the c^+ and c^- rays are both directed into the lock-exchange region). Otherwise, the spatial structure of the solution for $c_L^- < x/t < u_R$ is essentially like the free-boundary solution (Fig. 4c), consisting of an expansion fan and a constant-state following the right-going front.

At larger values of $r_{cr1} < r < r_{cr2} \approx 0.8953$, the spatial profile of the solution again has a constant-state attached to the dissipation-free front followed by the two expansion fans typified by the right-going characteristic Benjamin front case (e.g. Fig. 4b). This is illustrated for the case of $r = 0.7$ shown in Fig. 6b. However, unlike the free-boundary solutions, there is a second critical value of $r_{cr2} \approx 0.8953$ where the central constant-state coincides with the dissipation-free-front conditions. This occurs where the Riemann invariant satisfies $u^-(1/2) = 1/2$. The implication of this for values of r approaching the Boussinesq case, $r_{cr2} < r \leq 1$, is that solutions would seem to require c^- rays that cross. Mathematically, this situation is typically resolved by the appearance of a shockline at which two inbound rays can meet. However, we choose not to pursue the analysis further, as our computations suggest that the dissipation-free front is not realized at these larger values of r. The solution for $[u_R(r), h_R(r)]$ using the forced-boundary condition (3.16) is plotted on Fig. 5; clearly the right-going front is only slightly affected by the change in the left-going-front condition.

Finally we consider the solution procedure described in LRL (their §3). LRL solve the Riemann invariant equation (3.3) for $u^+(h)$ starting from the left-going condition (3.16) and look for a crossing with the Benjamin relation (2.7) to arrive at the right-going frontal parameters (u_R, h_R). For $r < r_{cr1}$ the LRL procedure is the same as the procedure that leads to the flow shown in Fig. 6a. However for $r > r_{cr1}$ we find that $c_c^+ < u_R$ implying that rays emanating from the left-going front do not reach the right-going front; hence in our construction of the solution for this case, the left-going rays from the right-going characteristic Benjamin front are necessary to complete the solution through the right-side expansion fan (Fig. 6b). Although it is possible to construct the solution for $r > r_{cr1}$ (Fig. 6c) following the LRL procedure, one would need some physical basis external to the SWE for assigning the derived frontal parameters (u_R, h_R) which, as for the left-going front, must be considered a forced-boundary condition. In the limit as $r \to 1$, the LRL procedure produces the solution $u = h = 1/2$ for $-1/2 < x/t < +1/2$ (LRL, their Figs. 11-12) and versions of the latter may be found in the literature dating back to the 1940s (Yih, 1965, pp. 134-138). As shown in Fig. 5, there is little difference in $u_R(r)$ produced by the present, the modified LRL or the LRL solutions to the SWE; the major difference is in $h_R(r)$ for $r_{cr} < r < 1.0$.

4. Numerical Simulations

To assess the solutions of the two-layer SWE presented in the previous sections, we proceed here to more general equations of fluid motion. In the present work we follow Étienne *et al.* (2005) who give the equations of motion for a mixture of two incompressible fluids of different densities. The fluid density is given by $\tilde{\rho} = \rho_h \Phi + \rho_l(1 - \Phi)$ or, nondimensionalizing by the density of the heavier fluid ρ_h, $\rho = r + (1 - r)\Phi$, where Φ is the heavier-fluid volume fraction and ρ_l is the density of the lighter fluid. Using the same nondimensionalization as used for the shallow-water equations in §2, the equations expressing conservation of mass of the mixture, mass of the denser fluid and momentum of the mixture are, respectively,

$$\frac{\partial u_i}{\partial x_i} = -\frac{(1 - r)}{r + (1 - r)\Phi}\frac{D\Phi}{Dt}, \tag{4.1}$$

$$\frac{D\Phi}{Dt} + \Phi\frac{\partial u_i}{\partial x_i} = \frac{1}{ReSc}\frac{\partial^2\Phi}{\partial x_i^2} \tag{4.2}$$

and

$$\rho\frac{Du_i}{Dt} = -\frac{\partial p}{\partial x_i} + \frac{2}{Re}\frac{\partial}{\partial x_j}[\lambda(\Phi)(e_{ij} - \frac{1}{3}\frac{\partial u_k}{\partial x_k}\delta_{ij})] - \frac{\rho}{1-r}\delta_{i3} \tag{4.3}$$

where $Re = \rho_h U H/\eta$ and $Sc = (\eta/\rho_h)/\kappa$ are respectively the Reynolds and Schmidt numbers, η is a constant reference value for the dynamic viscosity, κ is the diffusion coefficient (assumed constant) and $U = \sqrt{(1-r)gH}$. Étienne *et al.* (2005) let the dynamic viscosity $\mu = \eta\lambda(\Phi)$ to allow for either constant dynamic viscosity ($\lambda = 1$) or constant kinematic viscosity [$\lambda = r + (1-r)\Phi$] .

Seeking solutions that are as close as possible to the physical situation described by the two-layer SWE, we will focus on the limiting case $Sc \to \infty$, signifying zero cross-species diffusion. With the assumption of constant dynamic viscosity, Eqs. (4.1)-(4.3) simplify to

$$\frac{\partial u_i}{\partial x_i} = 0, \tag{4.4}$$

$$\frac{D\rho}{Dt} = 0 \tag{4.5}$$

and

$$\rho\frac{Du_i}{Dt} = -\frac{\partial p}{\partial x_i} + \frac{1}{Re}\frac{\partial^2 u_i}{\partial x_j^2} - \frac{\rho}{1-r}\delta_{i3} . \tag{4.6}$$

Equations (4.4)–(4.6) are the same as solved by Bonametti et. al. (2008) where it is noted (p. 451) that there is in effect a finite value of $Sc \approx O(10^3)$ due to the limitations of finite-differencing across the sharp change in ρ at the fluid-fluid interface. Again, in conformity with the SWE, we will assume stress-free conditions at the upper and lower boundaries. Hereinafter (4.4)–(4.6) are referred to as the Navier-Stokes (NS) equations.

As noted in the Introduction and in previous work, the interface separating the heavier- from the lighter-fluid flows is generally unstable; hence one expects a transition to turbulence beyond a critical value of Re, and therefore, turbulent stress between the two fluids. To avoid turbulent stresses, one might restrict attention to lower-Re (laminar) cases; however for a low-Re flow there would then be viscous stress between the two fluids. Hence stress between the fluids is a generally unavoidable difference between the NS and the SWE solutions for lock-exchange flow. In the present paper we will present solutions ranging from turbulent to laminar flow. Although the lock (Fig. 1) is in principle two-dimensional, turbulent motion is fundamentally three-dimensional and therefore we will explore solutions to (4.4)-(4.6) for variations in (r, Re) in both two and three dimensions. Details on the numerical-solution technique, grid resolution, solution verification, etc. are given in the Appendix.

a. Results and comparison with the SWE solutions

To facilitate comparison of the SWE solutions (§3) with the NS solutions, it is convenient to plot the latter as a function of x/t at a time long enough for the establishment of a statistically steady-state solution. Plotted in this way, long-wave features of the NS solutions stand out more clearly, and shorter-wave features, such as the leading-edge gravity currents are compressed, in analogue to the way they are represented in the SWE. Figures 7a, c and d show the density field $\rho(x/t, z)$ from two-dimensional simulations of

the cases $r = 1.0, 0.7$ and 0.4, respectively, with $Re = 10^4$, while Figs. 7b, d and e show the y-averaged density field $\overline{\rho}(x/t, z)$ from three-dimensional simulations for the same cases (all at $t = 16$). Beginning with the Boussinesq case $r = 1$, Fig. 7a indicates flow instability along the interface between the advancing fronts; however, without the ability to produce a turbulent cascade to smaller scales, the flow is dominated by large-scale 'billows'. In three dimensions, Fig. 7b shows that the two-dimensional instability is able to break down into three-dimensional turbulence which diffuses the interface. For the non-Boussinesq case $r = 0.7$, the two- and three-dimensional simulations in Figs. 7c and d, respectively, also indicate turbulent flow along the interface with a suggestion of a reduced level of turbulence for the left-going front. However for $r = 0.4$, the two- and three-dimensional simulations in Figs. 7e and f, respectively, indicate laminar flow for the left-going front and turbulent flow for the right-going front. This simulated disappearance of turbulence from the left-going front with decreasing r has been found in the laboratory and numerical studies reviewed in §1. Overlaid on the three-dimensional numerical solutions are the present and the LRL solutions to the SWE. Some general points of comparison follow.

Both the present and the LRL solutions of the SWE agree with the NS solutions in that the speed of the left-going front is independent of r while that of the right-going front is inversely proportional to r [the NS $u_R(r)$ data points, plotted in Fig. 5b, are generally slower than the SWE solutions]; the NS solutions all have $v_L \approx -0.5$ as in the LRL SWE solution as compared with $v_L = -0.527$ in the present SWE solution. The present SWE solution agrees with the NS solutions in that the interface generally slants from the upper left to the lower right in all cases while the LRL solution approaches a level interface as $r \to 1$. In both SWE solutions the right-going front thins with decreasing r in agreement with the NS solution. We note that the only 'zone of constant state' that clearly emerges in the NS solutions is the one attached to the left-going front for $r = 0.4$ in agreement with the LRL solution; otherwise the NS solutions exhibit an interface that slopes from upper left to lower right approximately linearly in the variable x/t. Denoting the height of the middle density contour by $\hat{h}$ and letting $\eta = x/t$, this linear dependence can be expressed as,

$$\hat{h}(\eta) = \hat{h}_L - (\hat{h}_L - \hat{h}_R)\frac{\eta - \eta_L}{\eta_R - \eta_L} \ . \tag{4.7}$$

Although it is difficult to identify unambiguously the parameters in (4.7) from the NS solutions, it seems clear that, for these solutions with $Re = 10^4$, $\hat{h}_L$ decreases with r, reaching the asymptotic limit $\hat{h}_L = 1/2$ between $r = 0.7$ and $r = 0.4$.

b. Discussion

In our judgement, the foregoing NS-SWE-solution comparison indicates only limited success for the SWE solutions. Aside from the gross agreements noted above, it seems clear there is an unfavorable comparison of the SWE $h(x/t)$ point by point with the NS $\hat{h}(x/t)$. The only place where such a comparison is reasonably favorable is for the left-going front for $r = 0.4$ for the LRL SWE solution. However even in this case it must be recalled that the condition (3.16) is externally 'forced' in that there are no characteristic curves that reach the event line $x/t = -0.5$ from the lock region (see Fig. 6). In the NS solution the evolving interface is obviously a free boundary as information must come from the lock region. One can reasonably infer that local nonhydrostatic effects must produce a propagation speed faster than that supported by the SWE for the conditions (3.16), however a more precise mathematical model for this effect is unknown to the authors.
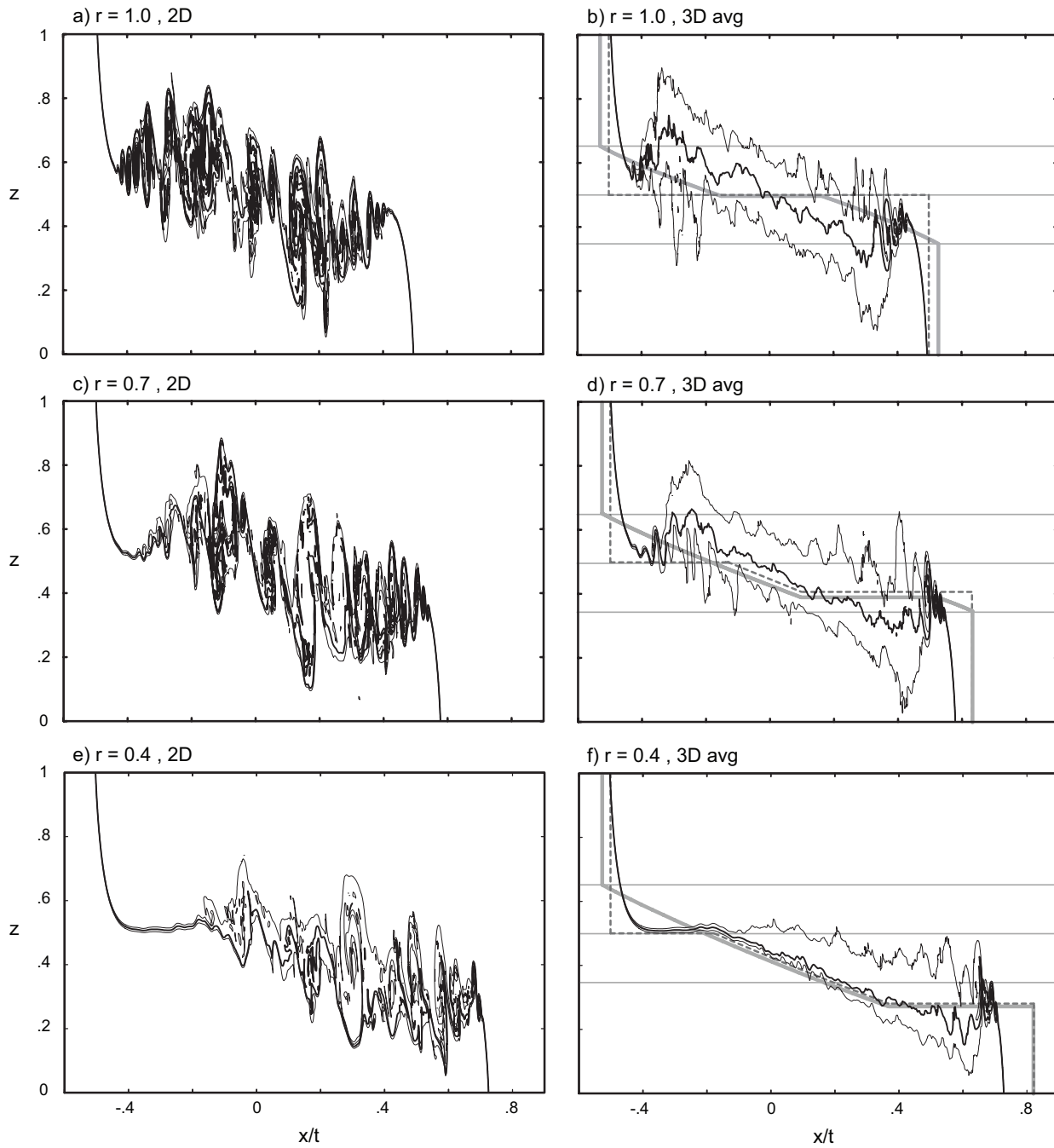
FIGURE 7. Navier-Stokes simulations of lock-exchange flow in two dimensions for density ratios $r =$ a) 1.0 , c) 0.7 and e) 0.4 and in three dimensions for $r =$ b) 1.0, d) 0.7 and f) 0.4. Shown from the three-dimensional simulations is the y-averaged density field. The three contour intervals displayed in all plots are 0.1, 0.5 and 0.9, with the middle value empasized. Overlaid on the three-dimensional solutions are the present solutions to the SWE (solid gray line) and those proposed by LRL (dashed gray line).

Accepting that there is an inherent tendency for the left-going front to satisfy the conditions (3.16), we investigate the conditions under which this occurs in the NS simulations. The tendency $\hat{h}_L(r) \to 1/2$ with decreasing r is also accompanied by a decrease in turbulence at the left-going front (Fig. 7). These results suggests a transition with decreasing r from a NS solution more akin to the present SWE solution ($h_L = 0.6527$ at a dissipative Benjamin front) to one more akin to the LRL SWE solution ($h_L = 0.5$ at a dissipation-free Benjamin front). To reinforce the point, we show in Fig. 8 the curve $\overline{\rho}(x,z)$ from the three-dimensional simulations (at $t = 16$) together with the potential-flow solution found in Benjamin (1968, his §4.3). A comparison across the range of r shows that, in the absence of turbulence (Fig. 8c), the NS solutions closely approximate the Benjamin potential-flow solution; however, as shown in Fig. 8a, in the Boussinesq case turbulence develops behind the 'head' producing a departure from the Benjamin potential-flow solution and a transition to a turbulent wake of reduced thickness. Somewhat counterintuitively it is the more viscous solution that approaches the potential-flow (inviscid) Benjamin solution. Indeed increasing the Reynolds number to $Re = 10^5$ for this case of $r = 0.4$ indicates instability and turbulence at the left-going front and a solution more akin to the present SWE solution (Fig. 9). Hence there is a strong indication from the present NS solutions that the character of the left-going front
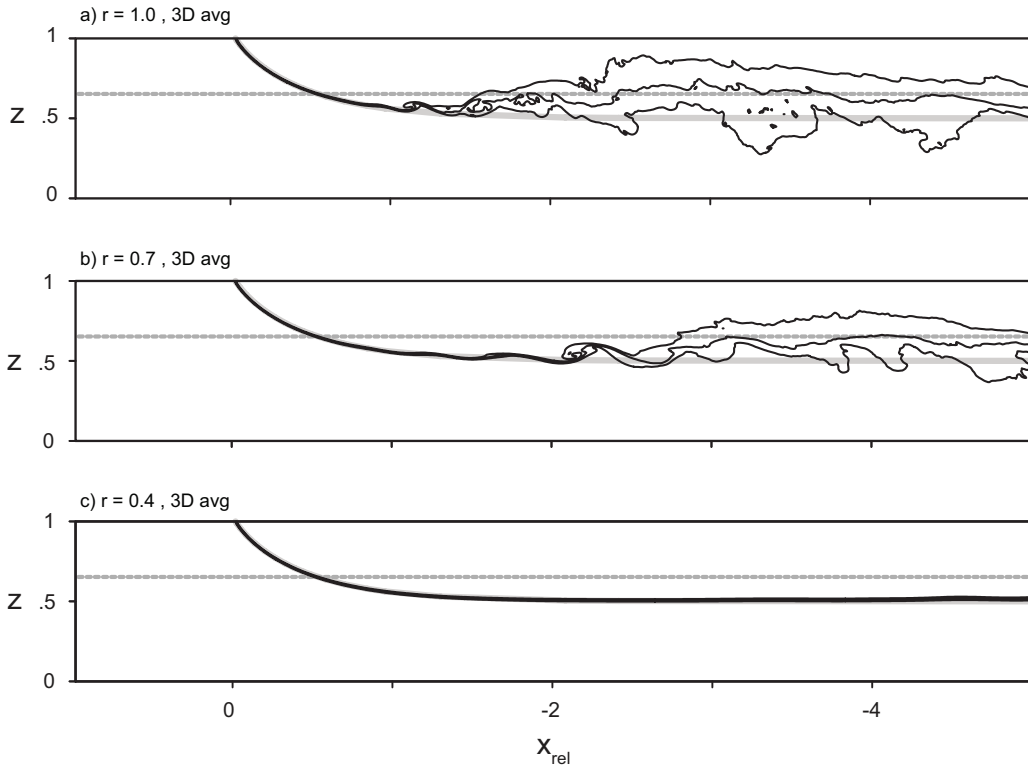

FIGURE 8. Across-channel-averaged density contours $0.1, 0.5$ and 0.9 plotted as a function of the distance relative to the left-going front x_{rel} at t= 16 from three-dimensional Navier-Stokes simulations of lock-exchange flow for $r =$ a) 1.0, b) 0.7 and c) 0.4 which correspond, respectively, to Figs. 7b, 7d and 7f. Overlaid is the interface as computed from Benjamin's potential-flow solution. The dotted lined denotes the thickness 0.347 for the left-going front according to the present theory.
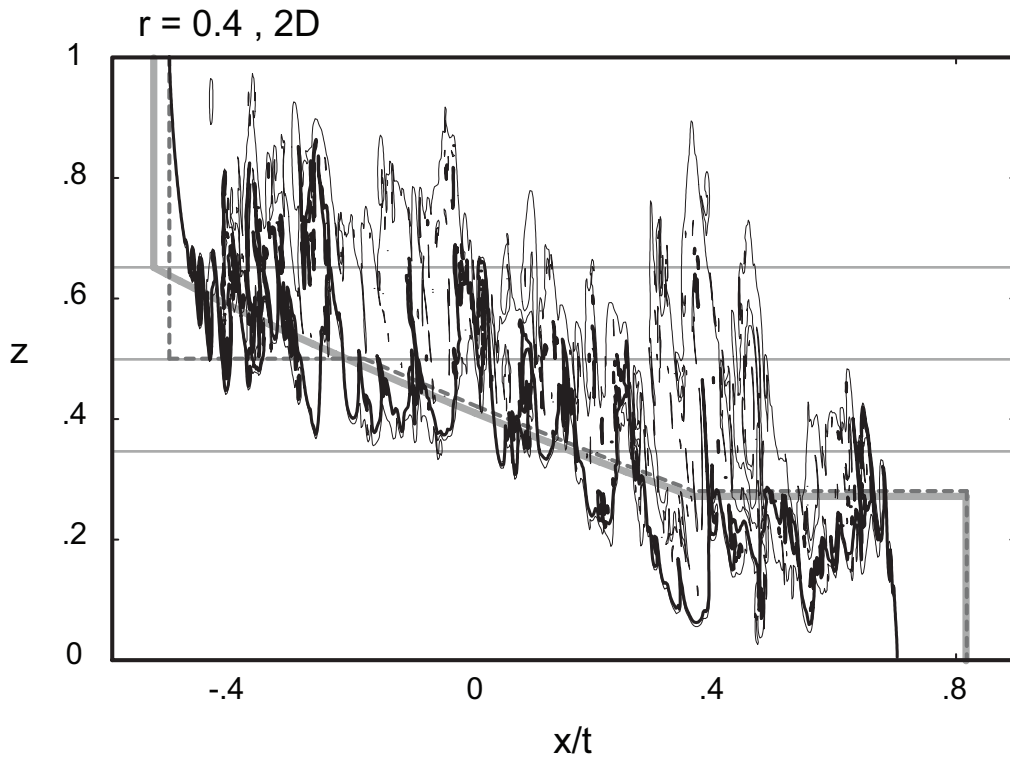
FIGURE 9. As in Fig. 7e, except for $Re = 10^5$; analytical solutions overlaid as in Fig. 7f.

depends on a critical Reynolds number that is a function of r. For $r \approx 1$ theory indicates the upper left-going current is unstable to disturbances of all wavelengths, but that as r decreases from unity, the longest wavelengths are stabilized (Benjamin 1968, p. 224-225; LRL, their Fig. 15a). Since viscous effects are strongest at the shorter wavelengths, and since longer wavelengths become stable for $r < 1$, it stands to reason that instability is suppressed for combinations of smaller r and smaller Re; the evidence from Fig. 8c is that viscous effects are large enough to suppress turbulence but not large enough to cause major departures from Benjamin's potential-flow solution for $r = 0.4$ and $Re = 10^4$.

The right-going frontal parameter $u_R(r)$ (Fig. 5a) from any of the SWE solutions compares rather well with the present NS solutions as well as those produced in 2D simulations by Bonometti et al. (2008) over a wider range of r. There is, however, significant disagreement between the present model and the LRL model right-going frontal parameter $h_R(r)$ for $r > r_{cr1}$ where the latter produces $h_R \to 1/2$ as $r \to 1$. In the latter case we believe the present model is closer to the NS solution in that Fig. 7b shows a significant overall tilt (from upper left to lower right) of $h(x/t)$ rather than the level interface $h(x/t) = 1/2$ predicted in the LRL SWE solution (see their Figs. 11-12 with $r = 1$).

5. Summary and Conclusions

Although the general sense of the circulation in lock-exchange flow is easily deduced from the initial baroclinic distribution of density and pressure, more precise detail on the

motion and nature of the evolving interface requires a fluid-flow model. In the present work we reviewed and advanced analytical models based on the shallow-water equations for non-Boussinesq lock-exchange flow. These analytical models were then compared with their counterpart numerical solutions based on the Navier-Stokes equations.

Nearly all of the existing analytical models of non-Boussinesq lock-exchange flow are based on the shallow-water approximation. Since the latter approximation fails near the leading edges of the mutually intruding flows (Fig. 1), front conditions must be given at both left- and right-going fronts in order to find solutions to the shallow-water equations. That a variety of such solutions exist in the literature is due to the individual investigators choice of front conditions (e.g. KRS and LRL); furthermore permitting discontinuous solutions between the two fronts gives an even greater variety of solutions (e.g. KC; see Fig. 4a of LRL). In KRS the shallow-water equations were solved numerically for the Boussinesq lock-exchange problem under the conditions that the left- and right-going fronts satisfy the Benjamin front conditions (2.6) and (2.7), respectively, and that the front is free boundary influenced by the motion within the lock region (i.e. it obeys 'causality'). The present paper has extended the KRS numerical solutions to cover non-Boussinesq flows (Fig. 2).

Using the method of characteristics, we have found exact analytical solutions (Figs. 3-5) that verify the numerical solutions of the shallow-water equations given here and in KRS. They also reinforce the finding that only solutions with frontal parameters implying dissipation at the fronts obey 'causality' in the shallow-water equations. However it has been noted in both laboratory and numerical experiments that the left-going front becomes less dissipative, taking the form of a potential-flow solution found by Benjamin (1968), as r, the ratio of lighter- to heavier-fluid density, decreases. Following LRL we have found analytical solutions of the shallow-water equations by imposing the dissipation-free condition on the left-going front. As noted in KRS, the dissipation-free front moves at a speed greater the shallow-water-equation wave speed and hence, from the point of view of shallow-water theory, must be considered a forced-boundary condition. For $r < r_{cr1} = 0.5532$, our solutions assuming a left-going dissipation-free front have rays emanating from the left-going front that impinge on the right-going front and thus determine the right-going frontal parameters; these solutions are the same as those of LRL (Fig. 6a). For $r > r_{cr1}$ we find that rays emanating from the left-going front do not reach the right-going front and that the solution must be completed with a right-going expansion fan (Fig. 6b). Notwithstanding that the left-going rays do not reach the right-going front for $r > r_{cr1}$, LRL continue to look for the intersection of the solution to the Riemann invariant equation (3.3) with the Benjamin front condition (2.7) to find the right-going frontal parameters; we have constructed analytical solutions (Fig. 6c), with the understanding that these must be regarded as solutions in which both the left- and right-going frontal parameters represent forced-boundary conditions.

In an attempt to authenticate the various solutions to the shallow-water equations, we have carried out both two- and three-dimensional numerical solutions of the Navier-Stokes equations for relatively large Reynolds number ($Re = 10^4$), very large Schmidt number ($Sc \gg 1$) and free-slip conditions at the upper and lower bounding surfaces. For $Re = 10^4$ and $r = 1$, the interface separating lighter and heavier fluid is generally turbulent; however, as found in recent numerical studies, the left-going front becomes less turbulent with decreasing r. In the present simulations with $Re = 10^4$, the left-going front is essentially laminar at $r = 0.4$ (Fig. 7e, f) and closely approximates the Benjamin potential-flow solution (Fig. 8c). A further experiment keeping $r = 0.4$ but with a larger

Re shows that the left-moving front is again turbulent (Fig. 9) suggesting there is a critical $Re_{cr}(r)$ that determines the character of the left-going front.

Comparison of the present (free-boundary) with the LRL (forced-boundary) solutions of the shallow-water equations with their counterpart numerical solution of the Navier-Stokes (NS) equations produced mixed results. Both the free and forced solutions reproduced the NS-solution features of left-going frontal parameters (v_L, d_L) independent of r, right-going front speed u_R increasing with r and right-going front height h_R decreasing with r. The present free-boundary theory produced $v_L = -0.527$ while the forced-boundary theory prescribed $v_L = -0.5$ which agrees closely with the NS solutions. On the other hand, in the limit as $r \to 1$, the forced-boundary theory gives the level interface $h(x/t) = 0.5$ between the left- and right-going fronts, while the present free-boundary theory gives an interface that is tilted from lower right to the upper left implying that both d_L and h_L are less than 0.5 in agreement with the NS solutions. We noted that the only place where the NS solutions produced a zone of constant state is in association with the forced-boundary dissipation-free front. Both free- and forced-boundary theories gives very similar predictions for $u_R(r)$.

In the generally nonhydrostatic NS solutions, the evolving interface is of course a free boundary whose motion must be influenced by the flow in the lock region. We are unaware of an analytical theory taking account nonhydrostatic effects and a density interface intersecting the rigid surfaces that can be used to explain the evolution from $t = 0$ to the time when the steadily propagating fronts are established in lock-exchange flow. In addition to explaining how information flows from the lock region to the fronts, such a theory may also shed light on why the the upper-front speed $v_L \approx -0.5$ across the range of r while the upper-front h_L clearly varies with r in the NS solutions (Fig. 7). It may also explain why NS front speeds are relatively insensitive to the interfacial dynamics—both two- and three-dimensional simulations (with very different versions of interfacial turbulence) give surprisingly similar predictions for frontal parameters (Fig. 5a).

Appendix. Details of the Navier-Stokes solver

Numerical integration of the Navier-Stokes (NS) equations (4.4)–(4.6) requires solution of an elliptic equation to determine pressure p. Solution techniques can be expensive in three dimensions with resolution high enough for adequately resolved direct numerical simulation (DNS), and can be difficult to implement effectively on modern distributed-memory computing systems. As an alternative, we replace the mass-continuity equation (4.4) with a prognostic equation for pressure. This procedure eliminates the need to solve an elliptic equation, but introduces the need to account for acoustic waves. The latter problem is addressed in the present study using the procedure developed by Klemp et al. (2007). Our derivation of an appropriate pressure equation follows Chorin (1967); herein, we assume p is a function of ρ only, and we invoke an artificial speed of sound $c_s \equiv dp/d\rho$, then using (4.4)–(4.5) we find

$$\frac{Dp}{Dt} = -\rho c_s^2 \frac{\partial u_i}{\partial x_i}.$$

We set $c_s = 10U$ to ensure that acoustic waves propagate much faster than the flow of interest.

The time-integration method and spatial discretization follow Bryan and Rotunno (2008, p. 548) except the subgrid turbulence parameterization of KRS is replaced by
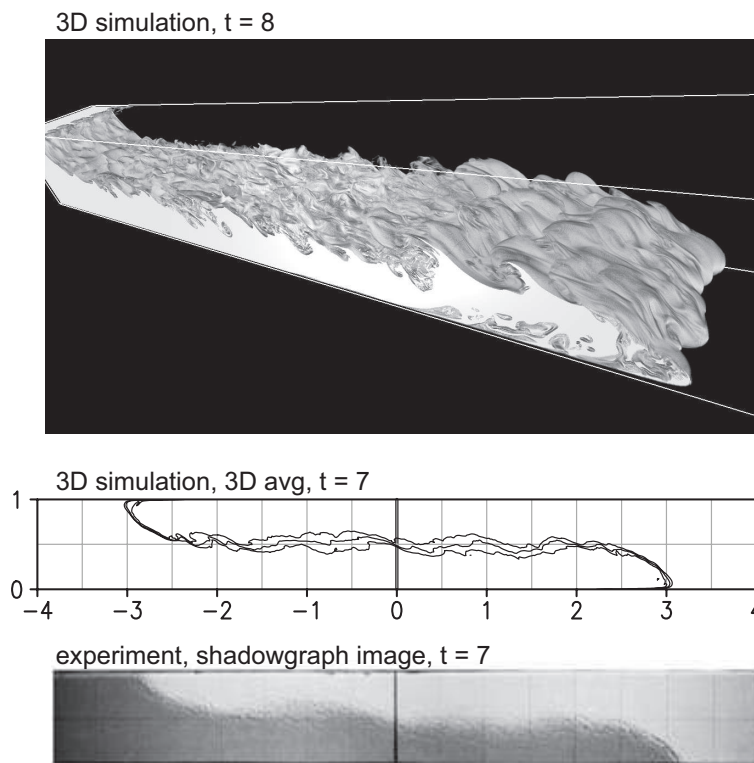
FIGURE A1. Direct numerical simulation of a Boussinesq lock-exchange laboratory experiment.

explicit stress-divergence calculations [second term on right side of (4.6)]. The domain extends from $x = -9$ to $x = +9$ for $r = 0.99$, from $x = -9$ to $x = +11$ for $r = 0.7$, and from $x = -9$ to $x = +13.5$ for $r = 0.4$. The initial "lock" is located at $x = 0$. All simulations extend from $y = 0$ to $y = 1$ and $z = 0$ to $z = 1$. Grid spacing is $1/320$ in all directions. Following previously published guidelines for consistency in DNS between resolution and Re (e.g., section 2.1 of Moin and Mahesh 1998), this resolution is considered sufficient for our nominal setting $Re = 10^4$.

Pressure at $t = 0$ is determined using (4.4) and (4.6). Because $u_i(t = 0) = 0$ everywhere and $\rho(t = 0)$ is a function of x only, then the elliptic equation that applies at $t = 0$ is

$$\frac{\partial^2 p}{\partial x^2} - \frac{1}{\rho}\frac{\partial \rho}{\partial x}\frac{\partial p}{\partial x} + \frac{\partial^2 p}{\partial z^2} = 0,$$

which is solved using successive over-relaxation.

To allow for development of three-dimensional motion in 3D simulations, small-amplitude random horizontal-velocity perturbations are added to the initial state. Slightly higher amplitude perturbations are inserted at $|x| < 0.1$ to crudely replicate laboratory experiments in which turbulent motions are created by abrupt removal of a partition at $t \approx 0$.

The solver is evaluated in two ways: comparison against a laboratory result, and comparison against previously published numerical simulations. For the first evaluation,

we run a three-dimensional simulation and compare against the Boussinesq lock-exchange experiment of Shin et al. (2004; SDL) (their Fig. 2). Our numerical simulation uses $r = 0.99$ and $Re = 10^4$, similar to values for SDL's experiment. No-slip boundary conditions are used for this simulation. Results at $t = 7$ are shown in Fig. A1, wherein the upper panel shows a view of the height of the middle density surface and the middle panel shows $\overline{\rho}(x, z)$ from the numerical simulation; the lower panel shows the shadowgraph image from SDL. The numerical simulation clearly captures the salient features of the experiment, such as: the propagation speed of the fronts; turbulent mixing along the interface; large eddies at $x \pm 0.75$ at $t = 4$; and a steeply sloped interface at $x = 0$ at $t = 7$.

For comparison against previously published results we simulate two-dimensional lock-exchange flow across a large range of r following Bonometti et al. (2008; BBM) (their Fig. 4). For these simulations we use the same settings as BBM: a domain of 25 $\times$ 1; $\Delta z = 1/160$; $\Delta x = 1/64$; and no-slip boundary conditions. BBM used a different method for nondimensionalization than we use herein; to allow direct comparison to their results we use $Re = 7071\sqrt{1 + r}$ and we examine the output at $t = 9\sqrt{1 + r}$. Results in Fig. A2 are comparable to those from BBM (their Fig. 4) in terms of overall structure and front propagation speeds.
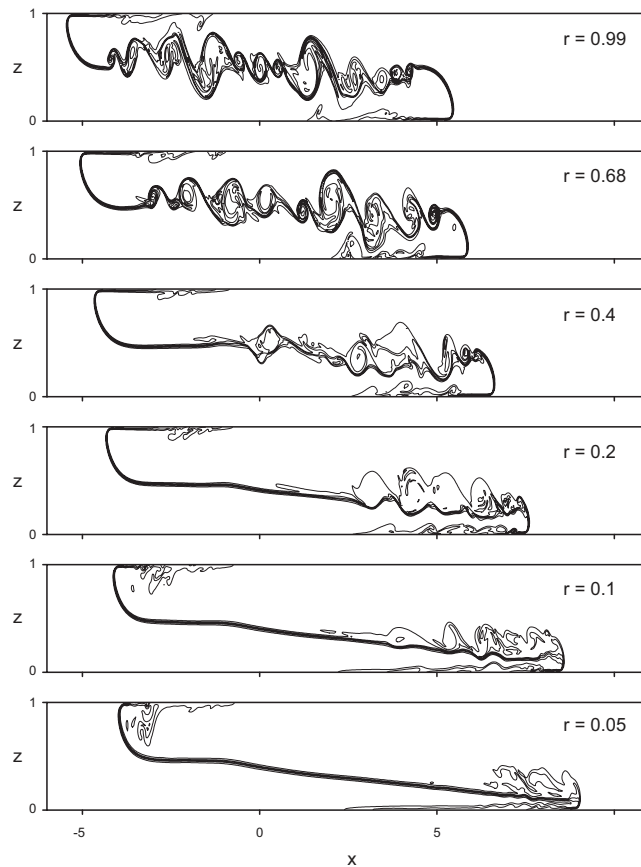

FIGURE A2. As in Fig. 4 of Bonometti et al. (2008).

REFERENCES

BENJAMIN, T. B., 1968: Gravity currents and related phenomena. *J. Fluid Mech.*, **31**, 209–248.

BIRMAN, V., MARTIN, J. E., & MEIBURG, E. , 2005: The non-Boussinesq lock-exchange problem. Part 2. High resolution simulations *J. Fluid Mech.*, **537**, 125–144.

BONAMETTI, T., BALACHANDAR, S. & MAGNAUDET, J., 2008: Wall effects in non-Boussinesq density currents. *J. Fluid Mech.*, **616**, 445-475.

BRYAN, G. H., & ROTUNNO, R., 2008: Gravity currents in a deep anelastic atmosphere. *J. Atmos. Sci.*, **65**, 536–556.

CHORIN, A. J., 1967: A numerical method for solving incompressible viscous flow problems. *J. Comput. Phys.*, **2,** 12–26.

ÉTIENNE, J., HOPFINGER, E. J., SARAMITO, P., 2005: Numerical simulations of high density ratio lock-exchange ows. *Phys. Fluids*, **17**, 036601.

GRÖBELBAUER, H. P., FANNELØP, T. K. & BRITTER, R. E., 1993: The propagation of intrusion fronts of high density ratios. *J. Fluid Mech.*, **250**, 669–687.

HÄRTEL, C., MEIBURG, E. & NECKER, F., 2000: Analysis and direct numerical simulation of the flow at a gravity current head. Part 1. Flow topology and front speed for slip and no-slip boundaries. *J. Fluid Mech.*, **418**, 189–212.

KELLER, J. J., & Y.-P. CHYOU, 1991: On the hydraulic lock-exchange problem. *J. Appl. Math. Phys*, **42**, 874–910.

KLEMP, J. B., ROTUNNO, R. & SKAMAROCK, W. C., 1994: On the dynamics of gravity currents in a channel. *J. Fluid Mech.*, **269**, 169–198.

KLEMP, J. B., SKAMAROCK, W. C., AND DUDHIA, J., 2007: Conservative split-explicit time integration methods for the compressible nonhydrostatic equations. *Mon. Wea. Rev.,* **135**, 2897–2913.

LOWE, R. J., ROTTMAN, J. W., & LINDEN, P. F. , 2005: The non-Boussinesq lock-exchange problem. Part 1. Theory and experiments *J. Fluid Mech.*, **537**, 101–124.

MOIN, P., & MAHESH, K., 1998: Direct numerical simulation: A tool in turbulence research. *Ann. Rev. Fluid Mech.*, **30**, 539–578.

ROTTMAN, J. W., & SIMPSON, J. E., 1983: Gravity currents produced by instantaneous releases of a heavy fluid in a rectangular channel. *J. Fluid Mech.*, **135**, 95–110.

SHIKHMURAZAEV, Y. D., 2008: *Capillary Flows with Forming Interfaces*, Chapman and Hall/CRC, 456 pp.

SHIN, J. O., DALZIEL, S., & LINDEN, P. F. , 2004: Gravity currents produced by lock exchange. *J. Fluid Mech.*, **521**, 1–34.

SIMPSON, J. E., & BRITTER, R. E., 1979: The dynamics of the head of a gravity current advancing over a horizontal surface. *J. Fluid Mech.*, **94**, 477–495.

WHITHAM, G. B., 1974: *Linear and Nonlinear Waves*, Wiley, 636 pp.

YIH, C.-S., 1965: *Dynamics of Nonhomogeneous Fluids*, Macmillan, 301 pp.

FIGURE 1. Schematic of lock-exchange flow based on a) laboratory data and b) typical solutions to the shallow-water equations. The vertical line at $\tilde{x} = 0$ indicates the lock center where the heavier and lighter fluids are initially separated; the horizontal channel walls are separated in the vertical by a distance H. After the release of the lock the heavier (lighter) fluid flows to the right (left) at speed $\tilde{u}_f$ ($\tilde{v}_f$) with thickness $\tilde{h}_f$ ($\tilde{d}_f$) measured some distance behind the complicated flow at the leading edge.

FIGURE 2. Numerical solutions of the two-layer shallow water equations with the front conditions (2.6)-(2.7) for $r = 1.0, 0.7$ and 0.4. For each r, the height of the interface is displayed in a), c) and e), and the layer and characteristic velocities (2.4) are displayed in b), d) and f).

FIGURE 3. Solution to the Riemann invariant equation (3.3) for $u^\pm(h)$ for density ratio $r =$ a) 1.0. b) 0.7 and c) 0.4. Starting values for the integrations of (3.3) are indicated by the points $u^- = u_R, h = h_R$ and $u^+ = u_L, h = h_L$. In a) and b), (u_c, h_c) denotes the crossing point where $u^+(h) = u^-(h)$ and the thick solid lines indicates the parts of the $u^\pm(h)$ solution curves relevant for calculating the corresponding characteristic velocities $c^\pm(u^+)$, $c^\pm(u^-)$ and upper-layer velocities $v^\pm$ (long-dashed curves). In c) there is no crossing point which indicates a change in character of the solution.

FIGURE 4. Analytical construction of the solution to the shallow water equations for density ratio $r =$ a) 1.0, b) 0.7 and c) 0.4. For each case the height of the interface h (upper panel) is plotted versus the combined coordinate x/t with the corresponding ray diagram given directly below. In a) and b) the zone of constant state where $h(x/t) = h_c$ (thin line segment) is located within the cone $c_c^- < x/t < c_c^+$ indicated in the ray diagram, and the left and right-side expansion fans (thick line segments) are defined by the ray-diagram cones $c_L^- < x/t < c_c^-$ and $c_c^+ < x/t < c_R^+$, respectively. In c) the right-side expansion fan disappears.

FIGURE 5. Right-side-front a) speed u_R, and b) height h_R, as a function of r. The present free-boundary solution (solid line) has two seqments separated by the dot at $r = r_{cr} = 0.5821$ indicating the density ratio dividing characteristic ($r > r_{cr}$) from time-like ($r < r_{cr}$) Benjamin fronts. Solutions with the forced-boundary condition $u_L = h_L = 1/2$ and free-boundary conditions for the right-side front (dashed line) have $r = r_{cr1} = 0.5532$ indicated by the star; the square at $r = r_{cr2} = 0.8953$ is the limiting density ratio beyond which continuous solutions do not exist for these assumed frontal conditions. The LRL solutions are same as the foregoing for $r < 0.5532$ but differ for $r > 0.5532$ (indicated by the solid gray line). The front-speed data from the present simulations are indicated by the '+' (2D) and the gray '×' (3D); data from the 2D simulations of Bonometti et al. (2008) are indicated by the circles.

FIGURE 6. Analytical construction of the solution to the shallow water equations for the forced boundary condition $u_L = h_L = 1/2$ and free-boundary conditions on the right-side front for a) $r = 0.4$ and b) $r = 0.7$; c) LRL solution for $r = 0.7$ with forced-boundary conditions at both left and right fronts.

FIGURE 7. Navier-Stokes simulations of lock-exchange flow in two dimensions for density ratios $r =$ a) 1.0 , c) 0.7 and e) 0.4 and in three dimensions for $r =$ b) 1.0, d) 0.7 and f) 0.4. Shown from the three-dimensional simulations is the y-averaged density field. The three contour intervals displayed in all plots are 0.1, 0.5 and 0.9, with the middle value empasized. Overlaid on the three-dimensional solutions are the present solutions to the SWE (solid gray line) and those proposed by LRL (dashed gray line).

FIGURE 8. Across-channel-averaged density contours $0.1, 0.5$ and 0.9 plotted as a function of the distance relative to the left-going front x_{rel} at t= 16 from three-dimensional Navier-Stokes simulations of lock-exchange flow for $r =$ a) 1.0, b) 0.7 and c) 0.4 which correspond, respectively, to Figs. 7b, 7d and 7f. Overlaid is the interface as computed from Benjamin's potential-flow solution. The dotted lined denotes the thickness 0.347 for the left-going front according to the present theory.

FIGURE 9. As in Fig. 7e, except for $Re = 10^5$; analytical solutions overlaid as in Fig. 7f.

FIGURE A1. Direct numerical simulation of a Boussinesq lock-exchange laboratory experiment.

FIGURE A2. As in Fig. 4 of Bonometti et al. (2008).